Paper 163

Proceedings of the Eleventh International Conference
on Computational Structures Technology,
B.H.V. Topping, (Editor),
Civil-Comp Press, Stirlingshire, Scotland

Elastic Buckling of Conical Shells under the Combined Loading of Axial Compression and External Pressure

J. Błachut and D. Stanier
Mechanical Engineering
The University of Liverpool, United Kingdom

Abstract

This paper details development of a test rig for buckling tests of shell components subjected to pressure and, or axial (centric or eccentric) loading. Test results were obtained for conical shells made from Mylar. These delivered interactive stability diagrams. The effect of off-axis axial compression on the buckling strength of pressurised cone is also given. Shape measurements provided information on the quality of tested models. The latter includes the magnitudes and positions of the inward and outward localised shape distortions. Experimental data is compared with numerical predictions of failure loads for the case of geometrically perfect models. The comparison of experimental results with numerically predicted buckling loads is poor. In addition to large imperfections other possible sources contributing to the large discrepancy between experimental and theoretical results are also discussed.

Keywords: interactive buckling, axial compression, external pressure, conical shells, eccentric loading, Mylar.

1 Introduction and Scope

The study of the phenomena of buckling in conical shells is a problem that can be of significance in industrial construction. They are often used within aerospace and marine industries where they experience a number of loading types (e.g., axial compression, internal/external pressure, edge shear force and torsion) and the design of the shell depends on a number of variables (e.g., the slant length, wall thickness, specimen height and cone semi-vertex angle), but very little design regulation is openly available for their construction, [1, 2].
A recent study into buckling tests which has been carried out on conical shells has listed about 600 tests during the last fifty years, [3]. Most of these tests were on shells subjected to a single load with a large proportion of results obtained on models made from Mylar. Combined stability of metallic cones was the main thrust

of investigations reported in Refs [3-5]. Mild steel conical shells were subjected to axial compression and external pressure. The work was centred on thick cones of $r_2/t = 34.0$ and 54.0, that failed in the elastic-plastic region (r_2 being the radius of a cone at its base). However, as far as the authors are aware, no such work has been done to understand the combined stability of conical shells that fail in the elastic region apart from the work reported in Ref. [6] which was an experimental study using Mylar as the test material. This established that there were significant differences in the buckling loads between experimental and theoretical results, and concluded this to be largely due to initial geometric imperfections in the specimens. However this report did not seek to quantify these imperfections.

It has been well established in early investigations, such as those reviewed for example in Refs [7-13], that imperfections in the geometry of shells can significantly reduce the buckling strength. There has been much work to establish these effects on shells of revolution, mainly concerning cylindrical shells however some have also looked at this effect more directly concerning conical shells. These have looked at the effects of imperfections that are either axisymmetric [11, 12], the effects of singular localised imperfections [13], or the effects of non-uniform axial length [15]. In a recent work, [16], the imperfections were measured on a number of mild steel conical specimens subjected to external pressure. Imperfection sensitivity of cones failing within the elastic-plastic domain is also discussed in Ref. [17].

The current paper describes a recently developed test rig that is used to examine the elastic stability of conical shells, subjected to combined axial compression and/or external pressure, constructed of Mylar. Measurements of the shell imperfections are discussed, and used to make comparisons to numerical results taken from ABAQUS [18] and BOSOR5 [19].

2 Experimentation

2.1 Test Apparatus

The test apparatus is depicted in Fig. 1 whilst Fig. 2 shows a schematic diagram of the rig and data recording equipment. The test specimen is 'press fitted' into the steel base-plate collar as it can be seen in Fig. 1, holding the cone's bottom flange in position during testing. The specimen is sat upon a base-plate which allows movement in the x and y directions, allowing alignment of the specimen and the potential for eccentric loading of the axial load (accuracy ± 0.2 mm).

The flange that the specimen is mounted on the base plate and it can be up to 200 mm in diameter, with a total allowable height of 190 mm (including both flanges).

The axial compressive load is applied by a screw jack, with a gear ratio of 10:1 (0.2 mm axial movement per revolution) allowing 110 mm of axial displacement applied to the top flange through the ball bearing in order to minimise any bending moment developed during the tests. This is suspended centrally above the specimen on top of a steel framework. This load is recorded by a 500 N load cell with a measured error of 0.07%. Load cells of smaller or larger range can also be used.

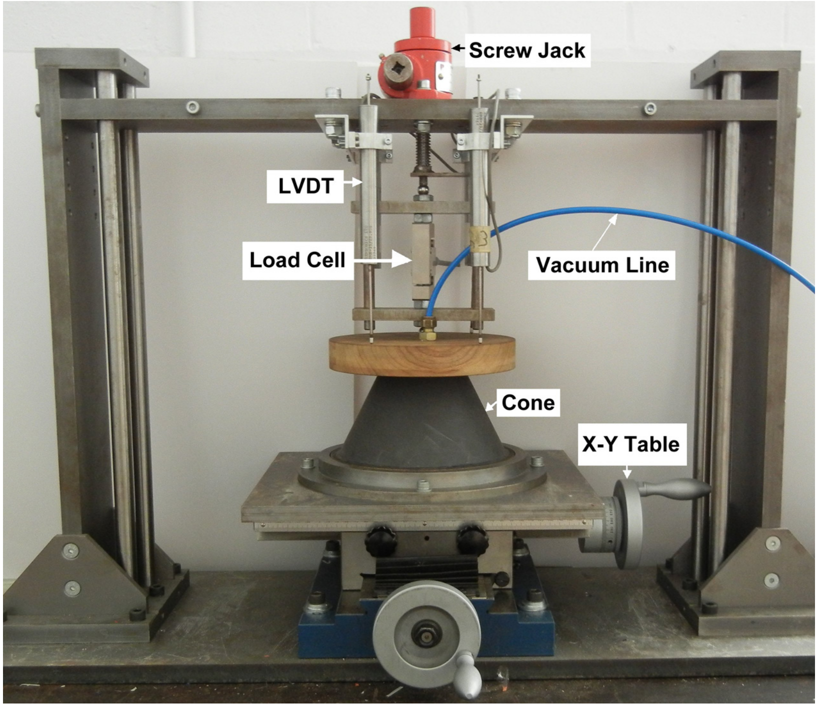

Figure 1: View of test rig, mounted model P2, four LVDs, load cell, and vacuum line.

The external pressure is applied to the specimen via a vacuum inside the specimen. It consists of a pump connected to two 20 litre vacuum tanks which help to steady the vacuum pressure when it is applied. At the moment, the system will reach a maximum vacuum of 87.7 kPa, which is applied to the specimen by slowly opening a tap valve that separates the specimen from the vacuum tanks. This load is recorded by a ± 0.1 kPa differential pressure transducer which is calibrated in the pressure range 0.0 kPa (atmosphere) to -60.0 kPa.

The axial displacements of the specimen are measured by four LVDT's placed equidistant around the circumference of the top flange of the specimens. These allow the displacement of the specimen to be verified as being vertical. It has also been seen that the wooden flanges compress during axial compressive testing and so a further two linear gauges are also used to measure this compression during tests. The LVDT's have been calibrated using slip-gauges produced to a tolerance of one micron, whilst the linear gauges have a guaranteed accuracy better than 15.0 microns, but will provide a value to 1.0 micron.

The measured data from the four LVDTs, the load cell and the pressure transducer is all recorded, against time, by a computer hardware and software package. This system allows the data collection frequency, range and total test time to be pre-determined and also allows for effective post-processing of the data. The data from the two linear gauges has to be manually recorded and correlated to the digitised data at this point in time.

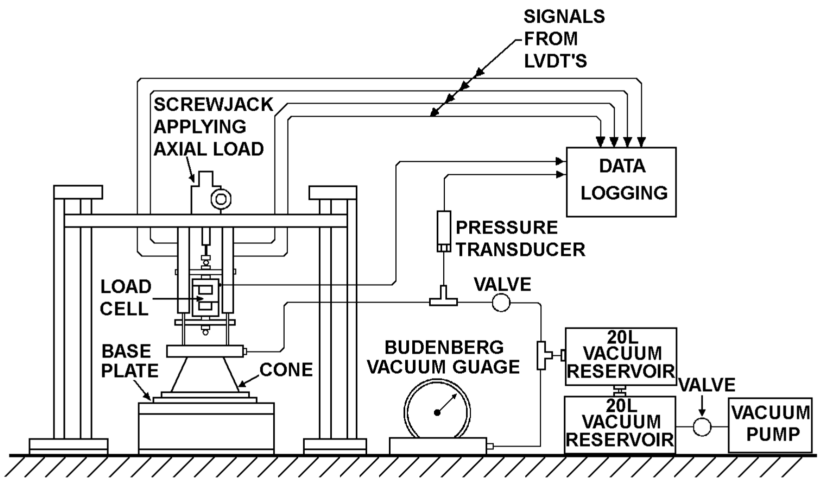

Figure 2: Schematic arrangements of the test rig and data measuring equipment.

2.2 Test Procedure

2.2.1 Axial compression

In applying axial compression the specimen is first aligned to the axis of the applied load, to ensure there is no eccentric loading. Then the screw jack is slowly turned, by hand, at a rate of about 1.0 mm/minute until buckling has occurred.

2.2.2 External pressure

In applying external pressure the vacuum tank is first loaded with a vacuum pressure of about 25.0 kPa, the vacuum pump is then switched off so that the analysis is quasi-static. The specimen is then attached to the vacuum system, with the specimen held firmly in the base-plate collar, and a tap valve is slowly opened allowing the external pressure to rise steadily. This is continued until buckling occurs.

2.2.3 Combined loading of axial compression and external pressure

This loading consists of firstly aligning the specimen to the axis of the applied load, and connecting it to the vacuum system. The vacuum system is then raised to around 25.0 kPa without applying this vacuum to the specimen, and the pump is switched off. The procedure then consists of increasing the axial load by turning the screw jack, until the prescribed magnitude of the compressive load is reached. The tap valve is then slowly released, increasing the external pressure applied to the specimen until failure whilst correcting the magnitude of axial force.

Testing has shown that it does not matter whether the external pressure or the axial compression is increased first; however the test rig is easier to operate in the manner previously described as it is easier to keep the axial load at a constant value whilst increasing the external pressure. As pressure is being increased a re-adjustment of axial force is required. This is in order to remove the increase of axial compression caused by the increase of pressure acting on the top flange. Hence, at any time the axial force acting on the top flange has two components: (i) mechanically applied compression via a ball bearing, and (ii) an external pressure induced force.

Cone	h	r_2	r_1	β	r_2/r_1	h/r_2	r_2/t
	mm			(°)			
P1	90.0	90.0	14.48	40.0	6.215	1.0	360.0
P2	90.0	90.0	45.0	26.565	2.0	1.0	360.0
P2a	90.0	90.0	45.0	26.565	2.0	1.0	360.0
P3	90.0	90.0	65.89	15.0	1.366	1.0	360.0
P4	90.0	90.0	82.13	5.0	1.096	1.0	360.0

Table 1: Nominal dimensions of tested cones.

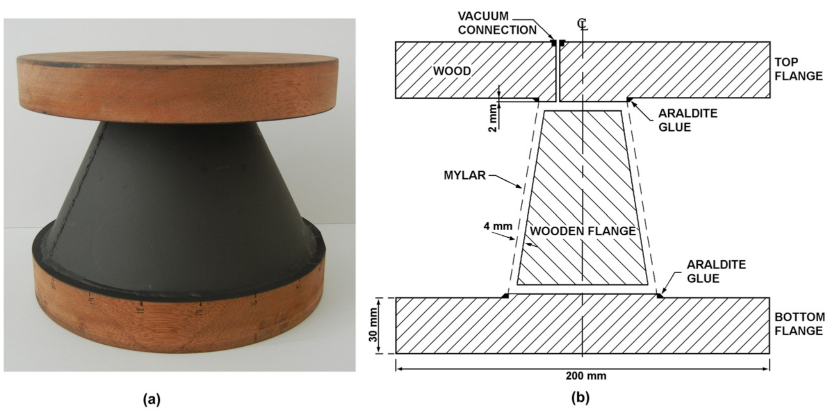

Figure 3: View of Mylar specimen P2a sprayed with graphite coating in order to obtain conducting surface (Fig. 3a). Exploded view of the test model is shown in Fig. 3b.

2.3 Manufacture of Specimens

Five Mylar truncated conical shells have been manufactured, measured, and tested under the simultaneous and independent action of axial compression and external pressure. The nominal dimensions of these specimens are given in Table 1. The conical shells have been selected to give a range of specimens varying in conicity; with the semi-vertex angle ranging from 5° (almost cylindrical) to 40° (highly conical) to determine the effects of conicity in comparison to cylindrical shells. The specimens have r_2/t values of 360.0 which are thin cones and are expected to fail in the elastic region. The specimens have wooden flanges to assist in applying the loads, with Mylar being wrapped around these and joined together by soldering a thin strip of Mylar down the seam. A typical specimen is shown in Figure 3a (model P2a).

Two hardwood top and bottom flanges are used to form the top and bottom boundaries of the specimen. The flanges are 30.0 mm thick with a 2.0 mm 'lip', as illustrated in Fig. 3b, that support the top and bottom of the specimens. The potting material used to attach the specimens to the flanges is Araldite. The specimens are made from 0.25 mm thick Mylar which is cut, using a scalpel, from a roll and soldered together to form the seam. The seam is formed by using a thin strip of Mylar and a soldering iron to melt the Mylar along the seam to create a solid join. Once cones were fixed to top and bottom flanges they were sprayed with a thin graphite layer (Graphite 33 Conductive Coating manufactured by Kontakt Chemie).

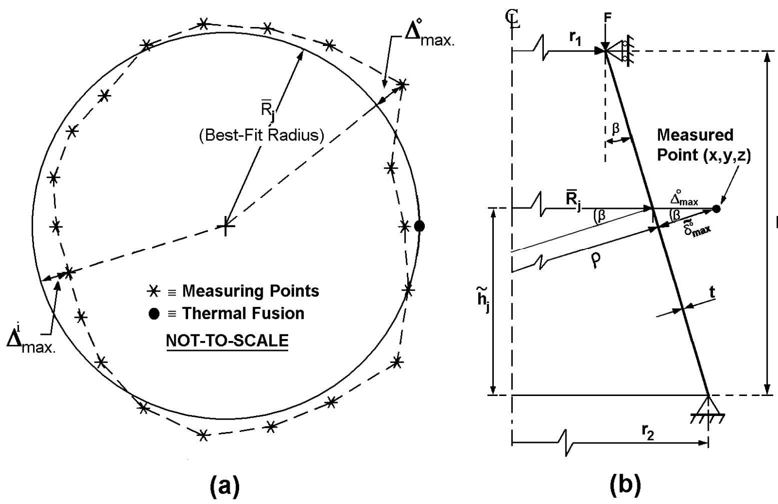

Figure 4: Magnified inward and outward, normal to the wall, deviations from the perfect geometry at half height (j = 7) for P2a model (Fig. 4a). Illustration of radial shape deviation, $\Delta^o_{\max}$, from best-fit radius, $\overline{R}_j$, and at height, $\widetilde{h}_j$ (Fig. 4b).

2.4 Shape Measurements

Next, cones were fixed in a lathe, centred, and (z, x) – co-ordinates of the outer surface were measured at 20 equally spaced meridians and at 7.5 mm distances along the slant. A very thin electric contact probe was used to measure the radial distance (see Ref. [3] for more details). A neon bulb lighted once the electric circuit was closed. This is a direct improvement on the method adopted in Ref. [22] where the contact probe exerted a force of 0.01 N onto the wall. In practical terms this 'electric-contact' approach meant that there was virtually no force exerted by the probe onto the cone's wall.

$\widetilde{h}_j$ (mm)	0.0	7.5	15.0	22.5	30.0	37.5	45.0	52.5	60.0	67.5	75.0	82.5	90.0
$\overline{R}_j$ (mm)	90.35	86.56	82.84	79.10	75.35	71.61	67.88	64.15	60.39	56.67	52.96	49.24	45.55
$\widetilde{\delta}^{o}_{\max}$ (mm)	0.755	0.68	0.606	0.469	0.525	0.567	0.612	0.619	0.645	0.548	0.523	0.394	0.313
$\widetilde{\delta}^{i}_{\max}$ (mm)	-0.57	-0.58	-0.59	-0.61	-0.61	-0.58	-0.60	-0.57	-0.53	-0.5	-0.44	-0.36	-0.27

Table 2: Maximum inward an outward shape deviations, $\widetilde{\delta}$, at different heights, $\widetilde{h}_j$, and related to the best fit radius, $\overline{R}_j$ (model P2a).

A number of shape approximations were tried. In the first instance the best-fit radii, $\overline{R}_j$, were found at each measuring height, $\widetilde{h}_j$, using the minimum of the sum of squares, where the residuals are given as $\Delta_k = \overline{R_j} - \sqrt{x_k^2 + z_k^2}$. The resulting best-fit radius, $\overline{R}_j$, based on n = 20 measured points for each height, $\widetilde{h}_j$, is

$$\overline{R_j} = \sum_{k=1}^{n=20} \sqrt{x_k^2 + z_k^2} \,/\, n \tag{1}$$

Figure 4a identifies the maximum outward, $\Delta^{o}_{\max}$, and maximum inward, $\Delta^{i}_{\max}$, deviations from best-fit circle at height, $\widetilde{h}_{j=7}$, and Figure 4b illustrates how the local outward deviation from best-fit radius was converted to the normal deviation, $\widetilde{\delta}^{o}_{\max}$. Table 2 provides the best-fit radii, $\overline{R_j}$, for all measured heights in model P2a. The corresponding maximum outward, $\widetilde{\delta}^{o}_{\max}$, and inward, $\widetilde{\delta}^{i}_{\max}$, departures from the best fit radii are given in Table 2. The same quantities are related to the percentage of cone's radius, ρ, and they are given in Table 3. It can be seen that the outward deviations vary from 0.53 % to 0.96 % of the local radius of curvature. The same ratio for the inward deviations varies from 0.56 % to 0.80 %.

In the subsequent step a set of 'the best-fit cones' was obtained. The process is now illustrated for model P2a. As the values of heights $\{\widetilde{h}_j$, j = 1, ..., 13}, were measured exactly and with the best-fit radii, $\{\widetilde{R}_j$, j = 1, ..., 13} being established, one could obtain the best-fit generator of the cone through the linear regression. The errors between the best-fit and measured pairs (x_k, z_k) can be written as:

$$e_k = z_k - a - bx_k \tag{2}$$

The minimization of the sum of the squares of residuals, e_k, i.e.:

$$\min_{a,b} \sum_{k=1}^{13} \left(z_k - a - bx_k \right)^2 \tag{3}$$

yielded a unique generator for the model P2a. The least-square fit for P2a is: z(x) = 181.3645 - 2.00844x.
It was however felt that a more realistic approximation of shape would be associated with shape deviations from each, of twenty measured, meridians. To this end, for each measured meridian the best-fit cone generator was obtained by using the linear regression – as outlined above – Eqns (1-2). Next, maximum outward, $\delta^o_{\max}$, and inward, $\delta^i_{\max}$, departures from straight, best-fit cone generator were extracted. Axial positions of $\left(\delta^o_{\max}, \delta^i_{\max}\right)$ were also identified. Table 4 provides the results which were obtained for all meridians in cone P2a. Finally, the largest magnitudes of $\left(\delta^o_{\max}, \delta^i_{\max}\right)$ seen in the whole model were stored. For model, P2a, they are provided in the last row of Table 4. Figure 5a plots the best-fit generator together with

$\widetilde{h}_j$ (mm)	0.0	7.5	15.0	22.5	30.0	37.5	45.0	52.5	60.0	67.5	75.0	82.5	90.0
$\widetilde{\delta}^o_{\max} / \rho_j$ (%)	0.75	0.70	0.65	0.53	0.62	0.71	0.81	0.86	0.96	0.86	0.88	0.71	0.62
$\widetilde{\delta}^i_{\max} / \rho_j$ (%)	0.56	0.60	0.64	0.69	0.72	0.73	0.79	0.80	0.79	0.79	0.75	0.66	0.54

Table 3: Maximum values of inward and outward shape deviations given as the $\left(\widetilde{\delta} / \rho\right)$-ratios, where ρ is the local radius of cone curvature (model P2a).

'measured data', and it shows the overall maximum inward and outward deviations. The above calculations were repeated for the remaining cones. The summary of best-fit results for all cones is given in Table 5 where the global shape deviations are given together with values of $\left(\overline{r}_2, \overline{r}_1, \beta\right)$. The latter are based on the use of cone generator associated with radial best-fit points at each measured height. This overall data given in Table 5 is used for numerical estimates of buckling loads discussed later on in the paper.

2.5 Mylar Properties

It is seen in Ref. [20] that there can be as much as ± 15% variation in the tensile modulus depending on the orientation of the material. However over time the quality of the Mylar has been improved by the manufacturers, with a later study (Ref. [21])

Meridian position (Degrees)	$\delta^{o}_{\max}$	$\delta^{i}_{\max}$	Height of maximum, $\widetilde{h}_j$	Height of minimum, $\widetilde{h}_j$	Best-fit slant angle
	(mm)				Degrees
0.0	0.224	-0.304	52.5	82.5	27.17
18.0	0.281	-0.328	52.5	82.5	26.75
36.0	0.134	-0.090	82.5	52.5	26.54
54.0	0.032	-0.024	82.5	45	26.57
72.0	0.046	-0.040	7.5	45	26.65
90.0	0.028	-0.016	82.5	52.5	26.65
108.0	0.016	-0.016	82.5	60	26.65
126.0	0.036	-0.024	82.5	45	26.72
144.0	0.054	-0.035	82.5	60	26.78
162.0	0.045	-0.033	82.5	37.5	26.80
180.0	0.035	-0.021	82.5	37.5	26.84
198.0	0.021	-0.010	82.5	60	26.85
216.0	0.019	-0.011	82.5	52.5	26.85
234.0	0.054	-0.032	82.5	52.5	26.85
252.0	0.062	-0.047	82.5	45	26.83
270.0	0.042	-0.040	82.5	45	26.76
288.0	0.008	-0.006	82.5	75	26.72
306.0	0.052	-0.029	7.5	37.5	26.70
324.0	0.150	-0.094	82.5	52.5	26.57
342.0	0.233	-0.240	52.5	82.5	26.78
Global maximum and minimum {Height - mm, Meridian – degrees}					
	0.281	-0.328	{52.5, 18.0}	{82.5, 18.0}	

Table 4: Maximum and minimum deviations, recorded for each of 20 measured meridians in shell P2a.

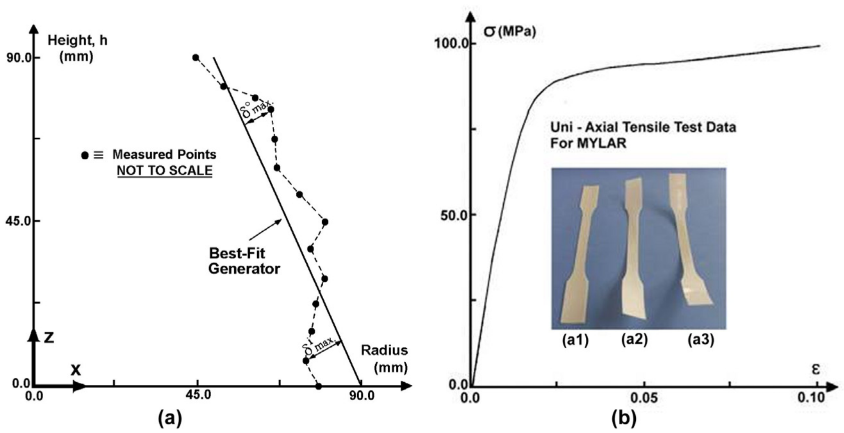

Figure 5: Average shape deviations along the best-fit shell generator (Fig. 5a). Uni-axial stress-strain curve for Mylar (Fig. 5b), and in the insert view of cut tensile specimens: (a1) ≡ along the length, (a2) ≡ at 45 deg to the length, and (a3) ≡ transverse to the length of MYLAR roll.

showing about 6 % variation. This has led many to regard the material as isotropic; however it is important to consider that the materials may vary, particularly dependent on the quality of the manufacturer.
The Mylar, used to manufacture the cones discussed in this paper, has been cut from the roll at 0.0^o (along the length), +45.0^o and 90.0^o (transverse to the length). The testing was performed using an extensometer at a strain rate of 1.0 mm/minute for the first 5 minutes and then increasing the strain rate to 4.0 mm/minute when past the proportional limit. It is taken 14 minutes to failure at this strain rate. Six tensile specimens were tested in this manner and the average Young's Modulus was found to be 6008.5 MPa at 0^o, 5738.0 MPa at 45.0^o and 5539.0 MPa at 90.0^o, showing about 8 % variation in the properties. This gives an average value of 5762.0 MPa, which when compared to the value found in Ref. [9] (E = 4826.0 MPa) is significantly higher – see Fig. 5b for average uniaxial experimental stress-strain curve. When the Mylar roll being used in this testing has been previously tested the results have been comparable to that of Ref. [6], indicating that the properties of the roll have changed (by about 16 %) over a period of approximately 10 years of storage.

	P1	P2	P2a	P3	P4
$\overline{r_2}$ (mm)	90.54	90.58	90.55	90.58	90.62
$\overline{r_1}$ (mm)	14.91	45.27	45.19	63.49	82.83
$\overline{\beta}$ (deg)	40.04	26.47	26.75	16.75	4.95
$\delta^o_{\max}\left(\widetilde{h}_j\right)$ (mm)	0.521 (52.5, 0.0)	0.223 (60.0, 0.0)	0.281 (52.5, 18.0)	0.346 (30.0, 0.0)	0.815 (90.0, 0.0)
$\delta^i_{\max}\left(\widetilde{h}_j\right)$ (mm)	-0.444 (7.5, 0.0)	-0.394 (90.0, 0.0)	-0.328 (82.5, 18.0)	-0.392 (90.0, 342.0)	-0.514 (53.75, 0.0)

Table 5: Best-fit geometry obtained from shape measurements of as-manufactured cones, P1, ..., P4. Values, $\left(\delta^o_{\max}\left(\widetilde{h}_j\right), \delta^i_{\max}\left(\widetilde{h}_j\right)\right)$, are global outward and inward departures from best-fit shell generator. Note: 52.5 mm ≡ height; 0.0 ≡ 0^o-meridian/slant.

3 Results

3.1 Centric Loading

Each of the cones was subjected to a series of buckling tests. The internal mandrel in each specimen prevented cones from being damaged during the buckling test. Figures 6 – 7 plot the results which were obtained. The first test was carried out under hydrostatic pressure and it is marked as point no. 1 in Fig. 6b. The subsequent test points covered the whole domain 'evenly' – as it can be seen for model P2 in

Fig. 6b. In this case, the final test was carried out for pure axial compression (point no. 10, Fig. 6b). As it was mentioned earlier the axial compression was applied first and this was followed by the application of slowly increasing pressure (vacuum). The magnitude of the axial force was continuously re-adjusted in order to compensate for the increasing pressure. The load deflection curves for model P2 are shown in Fig. 8, where the measured deflection, δ, is the axial movement of the top flange.

It can be seen from Figs 6 - 7 that the combined stability domains remain convex for all values of the semi-vertex angle, β. Experimental buckling loads: (i) F_o, for pure axial compression, and (ii) p_o, for pure external pressure were used to normalize the test results shown in Figs 6 - 7. The exact magnitudes of loads at which buckling occurred are given in Table 6. It can also be seen from Table 6 that an additional specimen, designated as P2a, has been added. This is a nominally identical cone to P2 model. The interactive diagram for this model is shown in Fig. 9a whilst Fig 9b shows a typical buckling mode corresponding to pressure only loading. It can be seen from Table 6 that model P2a had higher buckling axial force than model P2 (increase from 412.3 N to 499.3 N), and higher buckling pressure (increase from 1.313 MPa to 1.358 MPa). This indicates that manufacturing of nominally identical shells may not necessarily lead to good repeatability of test results. One explanation of this discrepancy might be associated with variability of Mylar properties. The exact orientation of Mylar blanks was not monitored at the time of manufacturing the models. It was only after uni-axial tests of flat coupons when it has become obvious that the cutting pattern of blanks could affect the buckling strength of cones.

3.2 Eccentric (Off-axis) Loading

In practice, the vertical compressive load can shift from the centre. This will create uneven loading of a shell. The effect of controlled off-axis loading on buckling strength of cone P2a, subjected to simultaneous action of external pressure (vacuum)

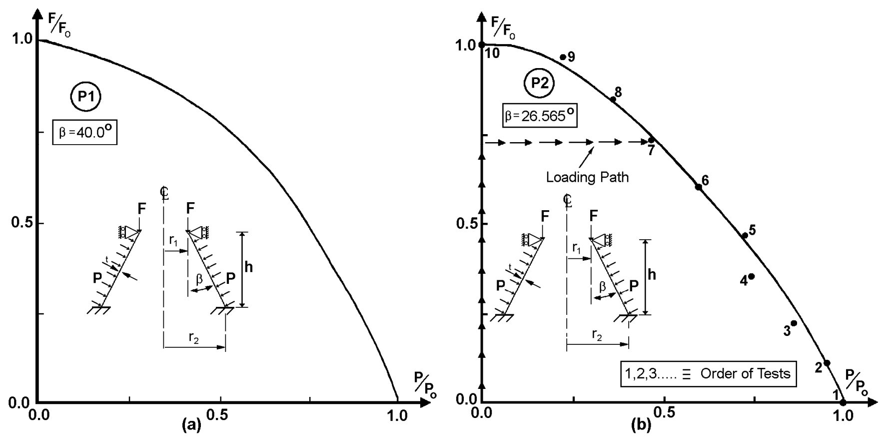

Figure 6: Interactive stability domain obtained for models P1 and P2. The order of experimental buckling tests is explicitly shown for specimen P2.

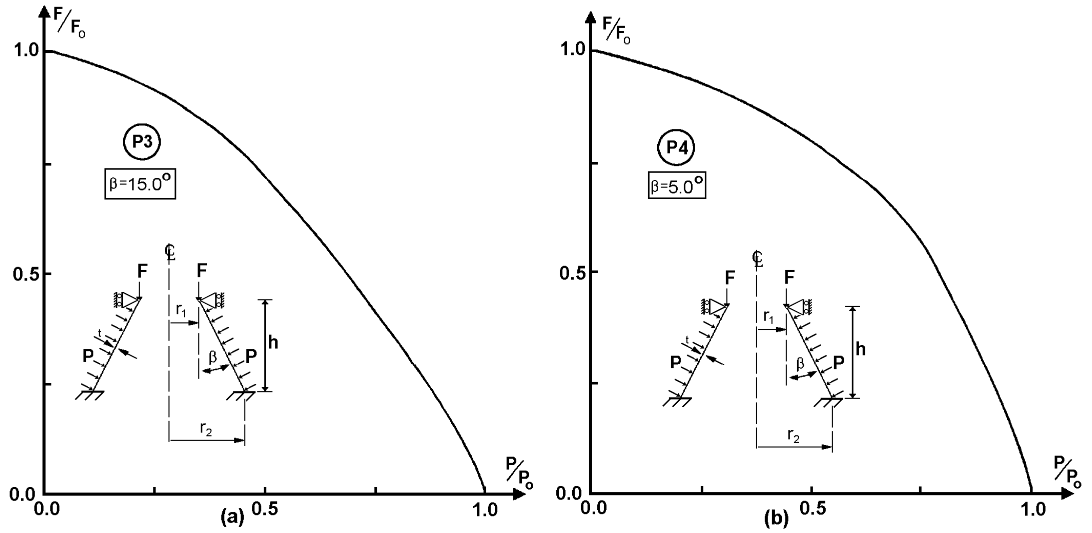

Figure 7: Interactive diagrams for models P3 and P4.

and axial compression was examined next. Two values of pre-set axial force were chosen, i.e., F = 125.0 N and F = 325.0 N. After loading to a pre-set value, the buckling pressure was established for various values of the off-set distance, r, - as illustrated in Fig. 10. Results which were obtained are plotted in Fig. 10 as curves 'A' and 'B'. The buckling pressure for each curve is normalized by the buckling pressure for the on-axis, centric loading. For the case of F = 125.0 N, the on-axis buckling pressure was, p_o = 1.068 kPa. The second case, (F = 325.0 N, p_o = 0.747 kPa) corresponds to point no. 2 in Fig. 9a.

It can be seen from Fig. 10 that as the value of 'r' increases the magnitude of buckling pressure decreases. For the case (F = 125.0 N, p_o = 1.068 kPa), the cone is able to support not only the axial compression, F = 125 N but a non-zero pressure, p = 0.5875 kPa when the load is applied at r/r_1 =1.0. For the case of larger force, F = 325.0 N, the pressure dropped much faster as the eccentricity was increased. For, r/r_1 = 0.898, the cone was unable to support any external pressure as it buckled under the application of the force, only.

4 Numerical Calculations – Comparison of Results

It is seen from Tables 4 and 5 that the magnitude of both the outward (positive) and inward (negative) shape distortions is large. In terms of the (amplitude-to-the-wall-thickness)-ratios, δ/t, they vary as follows: $0.89 \le \frac{\delta^o_{\max}}{t} \le 3.26$, and $-1.31 \le \frac{\delta^i_{\max}}{t} \le -2.06$ for the outward and inward distortions, respectively. Past work suggests that the inward shape deviations are responsible for the large reduction of buckling loads in conical shells, Ref. [11]. A recent study has shown

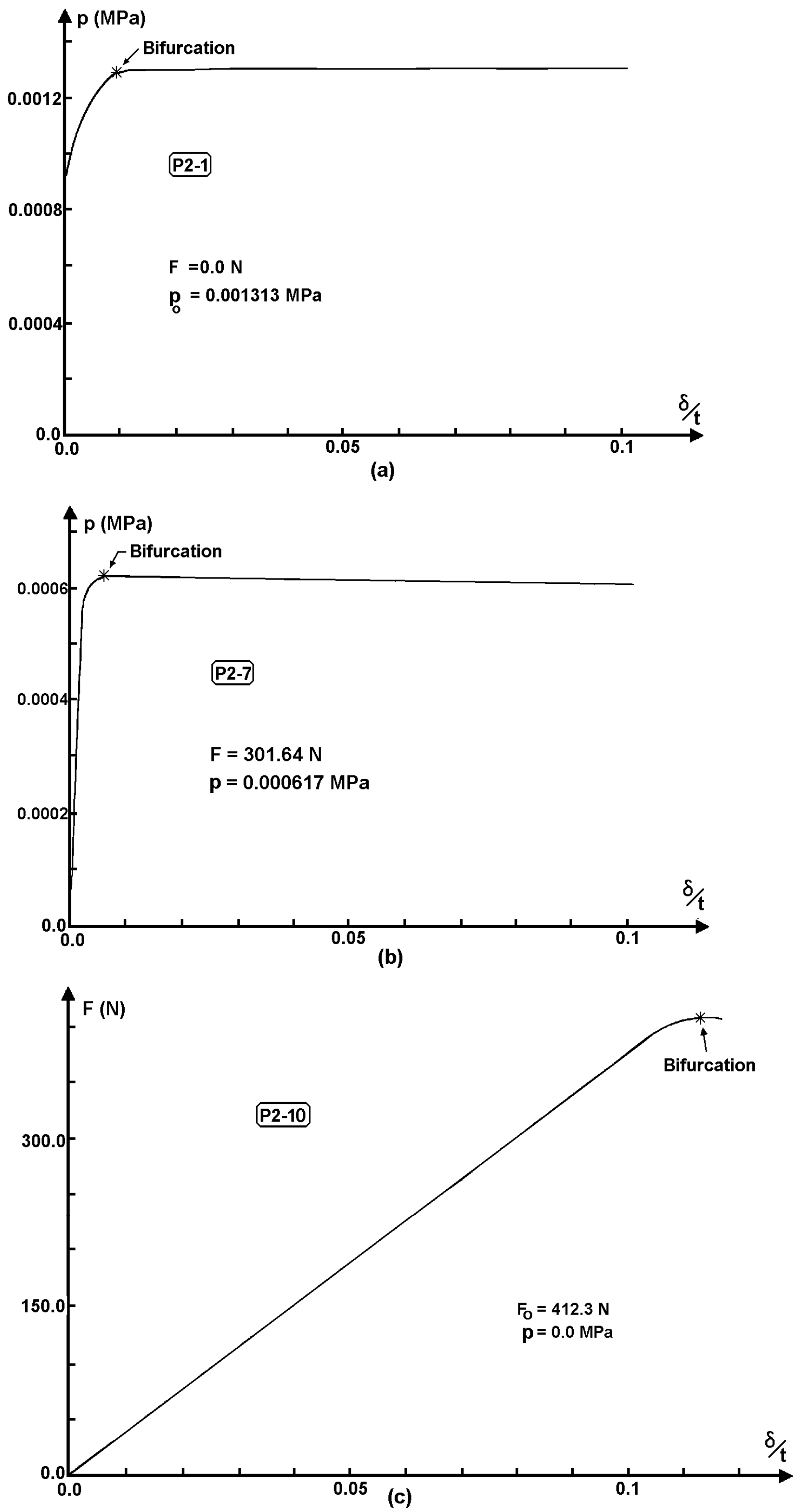

Figure 8: Experimental load deflection curves for model P2 at points 1, 7, and 10 from Fig. 6b. Bifurcation buckling is indicated for each combination of loading, i.e., for pressure only, combined loading, and for axial compression.

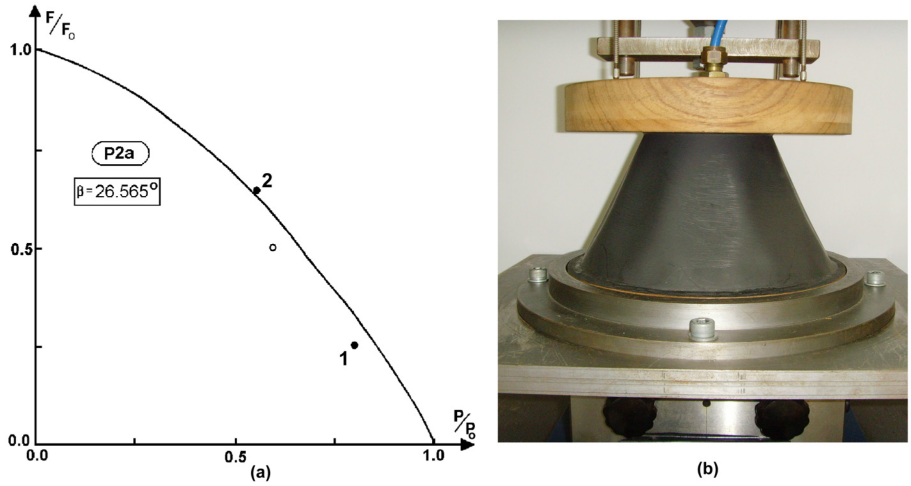

Figure 9: Interactive diagram for model P2a, (Fig. 9a). View of buckled cone P2a shown in Fig. 9b.

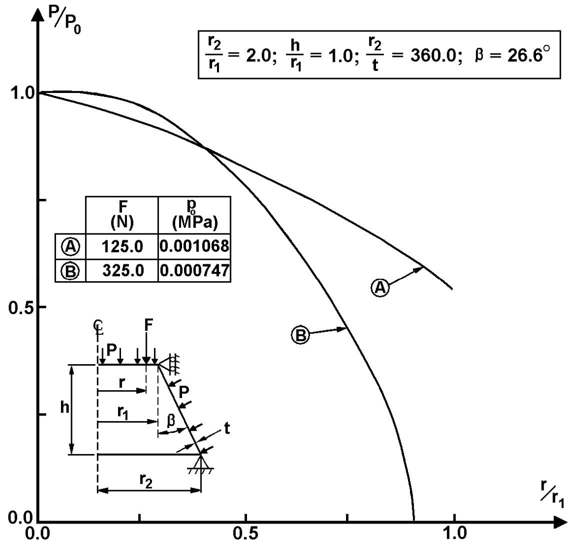

Figure 10: Variation of buckling pressure for two off-axis constant values of axial force, F (model P2a).

that outward shape deviations are equally dangerous, Ref. [23]. Nevertheless in the current paper numerical predictions of buckling load have been carried out for geometrically perfect cones, only. The FE results were obtained for the same load combinations as those given in Table 6, i.e., along the entire interactive plot. The axial force was applied first and it was kept constant whilst buckling pressure was sought along the single incremental path. The corresponding numerical values are expressed as $\left(\frac{F_{numerical}}{F_{experimental}}, \frac{p_{numerical}}{p_{exprimental}}\right)$ - ratios and they are given in Table 7. For all

P1	P2	P2a	P3	P4
{F[N], p[kPa]}				
{1.05, 1.599}	{8.35, 1.313}	{8.64, 1.358}	{15.39, 1.128}	{24.52, 1.157}
{43.73, 1.486}	{52.44, 1.246}	{54.73, 1.258}	{60.75, 1.052}	{69.89, 1.104}
{88.34, 1.431}	{99.70, 1.132}	{108.99, 1.116}	{108.44, 0.971}	{118.75, 1.057}
{140.89, 1.242}	{151.54, 0.975}	{170.37, 1.022}	{157.27, 0.892}	{168.23, 0.994}
{188.38, 1.10}	{197.98, 0.951}	{206.54, 1.038}	{208.71, 0.734}	{219.70, 0.955}
{244.18, 0.939}	{251.64, 0.782}	{266.84, 0.865}	{254.60, 0.645}	{266.52, 0.806}
{294.67, 0.664}	{305.56, 0.617}	{330.26, 0.747}	{302.14, 0.531}	{314.34, 0.754}
{346.85, 0.0}	{352.41, 0.476}	{368.82, 0.629}	{350.29, 0.417}	{360.74, 0.589}
	{400.95, 0.295}	{416.72, 0.377}	{400.00, 0.0}	{423.65, 0.0}
	{412.30,0.0}	{499.30, 0.0}		

Table 6: Experimental buckling loads for MYLAR cones. Note: underlined values were kept constant during tests.

P1	P2	P2a	P3	P4
$\{\frac{F_{numerical}}{F_{experimental}}, \frac{p_{numerical}}{p_{experimental}}\}$				
{1.0, 2.46}	{1.0, 2.77}	{1.0, 2.71}	{1.0, 2.94}	{1.0, 2.56}
{1.0, 2.64}	{1.0, 2.86}	{1.0, 2.86}	{1.0, 3.08}	{1.0, 2.61}
{1.0, 2.56}	{1.0, 3.07}	{1.0, 3.15}	{1.0, 3.25}	{1.0, 2.65}
{1.0, 2.96}	{1.0, 3.49}	{1.0, 3.33}	{1.0, 3.45}	{1.0, 2.74}
{1.0, 3.20}	{1.0, 3.49}	{1.0, 3.20}	{1.0, 4.09}	{1.0, 2.76}
{1.0, 3.62}	{1.0, 4.14}	{1.0, 3.70}	{1.0, 4.53}	{1.0, 2.98}
{1.0, 4.82}	{1.0, 4.99}	{1.0, 4.12}	{1.0, 5.35}	{1.0, 3.34}
{2.13, 0.0}	{1.0, 6.47}	{1.0, 4.77}	{1.0, 6.62}	{1.0, 4.14}
	{1.0, 9.83}	{1.0, 9.63}	{2.91, 0.0}	{2.98, 0.0}
	{2.48, 0.0}	{2.02, 0.0}		

Table 7: Comparison of experimental and numerical buckling loads. Note: underlined values were kept constant during the FE calculations and equalled to the exact experimental values.

cones under axial compression, only – the FE predictions are higher than the experimental results. The ratios of $\frac{F_{numerical}}{F_{experimental}}$ are 2.13, 2.48, 2.91, and 2.98 (from Table 7). This appears to be excessive but it is seen from Table 5 that all models had the largest recorded, dimple-type shape deviations close to the top flange. It is not unexpected to see such differences between the experiment and theory (see, for

example, Refs [2, 5, 8, 11, 23]). Similar range of discrepancy was recorded for models subjected to pressure, only (2.46, 2.27, 2.71, 2.94, 2.56). It is seen that under pressure loading the discrepancies are similar to those obtained under pure axial compression. Again, it is not surprising given the magnitude of initial shape imperfections.
Generally, there has been less research into stability of shells subjected to combined loading. As a result there is less information available on imperfections sensitivity under combined loading (axial compression and external pressure in this case). It is seen in table 7 that when axial force applied is 'high' (reasonably close to buckling level), the resulting external pressure is much smaller than the predicted values. The corresponding magnitudes seen in Table 7 vary from 4.14 to 9.83, and this raises the question how realistic the numerical predictions are. It is worth noting that these discrepancies become much smaller for lower magnitudes of axial forces. The source of these large discrepancies has not been established.

4 Conclusions

Stability of shells under combined loading is very important from a practical point of view. Reliable experimental data is difficult to obtain and, or interpret. The current paper has highlighted a number of problems which it would be worth investigating further. For example, the long term storage of Mylar material, traditionally and frequently used in elastic buckling tests, indicates that the elastic properties are likely to be affected. It has been noticed that the long term storage in a roll induces permanent distortion of Mylar. The sheets can easily be made flat – but the embedded residual strains appear to affect the shape of test models (cones in our case). The paper shows how this can result in dimple-type localized distortion with the depth of several wall thicknesses. With the Mylar sheet being 0.25 mm thick these shape deviations are difficult to see and they can only surface once the shape is carefully measured.

The eccentric loading has shown that deviations of the axial compression from the axis of symmetry by 5 % - 10 % of the top-end radius of the cone have not led to a dramatic loss of the load carrying capacity. However due to the above concerns about the properties/quality of Mylar material, these results are only indicative.

References

[1] ASME 'Code Case 2286-2, Alternative rules for determining allowable external pressure and compressive stresses for cylinders, cones, sphere and formed heads, Section VIII, Divisions 1 and 2', Cases of the ASME Boiler and Pressure Vessel Code, ASME, New York, 2008 edition, pp. 1 -13.

[2] ECCS TC8 TWG 8.4 Shells, 'Buckling of steel shells – European design recommendations', No. 125, 384p, 5th edition, ECCS, Multicomp Lda, Portugal, 2008, (ISBN 92-9147-000-92).

[3] O. Ifayefunmi, "Combined stability of conical shells", PhD Thesis, The University of Liverpool, 2011.
[4] J. Błachut, O. Ifayefunmi, "Plastic buckling of conical shells", Journal of Offshore Mechanics and Arctic Engineering, 132(041402), 1-11, 2010.
[5] J. Błachut, "Interactive plastic buckling of cones subjected to axial compression and external pressure", Ocean Engineering, 2012 (in print).
[6] V.I. Weingarten, P. Seide, "Elastic stability of thin-walled cylindrical and conical shells under combined external pressure and axial compression", AIAA Jnl, 3(6), 913-920, 1965.
[7] J.G. Teng, "Buckling of thin shells: recent advances and trends", Applied Mechanics Reviews, Transactions of the AMSE, 49, 1991, 263-274.
[8] J. Singer, J. Arbocz, T. Weller, "Buckling experiments: experimental methods in buckling of thin-walled structures", vol. 2, John Wiley & Sons Inc., New York, 2002.
[9] V.I. Weingarten, E.J. Morgan, P. Seide, "Elastic stability of thin-walled cylindrical and conical shells under axial compression", AIAA, 3(3), 500-505, 1965.
[10] V.I. Weingarten, E.J. Morgan, P. Seide, "Elastic stability of thin-walled cylindrical and conical shells under combined internal pressure and axial compression", AIAA Jnl, 3(6), 1118-1125, 1965.
[11] J. Arbocz, "Buckling of conical shells under axial compression", NASA CR-1162, Washington, D.C., USA, September 1968, 52p.
[12] P.A. Cooper, C.B. Dexter, "Buckling of a conical shell with local imperfections", NASA Technical Memorandum, NASA TM X-2991, 1974.
[13] C.G. Foster, "Axial compression buckling of conical and cylindrical shells", Experimental Mechanics, 27(3), 255-267, 1987.
[14] A.A. El Damatty, R.M. Korol, F.A. Mirza, "Large displacement extension of consistent shell element for static and dynamic analysis", Computers and Structures, 62(6), 943-960, 1997.
[15] J. Błachut, "Buckling of axially compressed cylinders with imperfect length", Computers and Structures, 88(5-6), 365-374, 2010.
[16] B.S. Golzan, H. Showkati, "Buckling of thin-walled conical shells under uniform external pressure", Thin-Walled Structures, 46(5), 516-529, 2008.
[17] J. Zielnica, "Imperfection sensitivity and stability of an elastic-plastic conical shell under axisymmetric loading", Archive of Applied Mechanics, 72(6-7) 395-417, 2002.
[18] Hibbitt, Karlsson, Sorensen Inc. ABAQUS manual, ver. 6.4, Pawtucket, RI 02860-4847, USA, 2005.
[19] D. Bushnell, "BOSOR5: Program for buckling of elastic-plastic complex shells of revolution including large deflections and creep", Computers and Structures, 6(3), 221-239, 1976.
[20] O. Ishai, T. Weller, J. Singer, "Anisotropy of Mylar A sheets", ASTM Journal of Materials, 3(2), 337-351, 1968.
[21] N. Yamaki, K. Otomo, "Experiments on the postbuckling behaviour of circular cylindrical shells under hydrostatic pressure", Experimental Mechanics, 13(9), 299-304, 1973.

[22] N. Yamaki, "Elastic stability of circular cylindrical shells", North Holland, Amsterdam New York, 558p, 1984.
[23] J. Błachut, "Buckling of truncated cones with localized imperfections", In Proc. of the ASME 2012 Pressure Vessel and Piping Conference PVP2012, July 2012, Toronto, PVP2012-78384, pp. 1-9, ASME, NY, 2012.